Demonstration of Aerosol Property Profiling by Multiwavelength Lidar under Varying Relative Humidity Conditions

I. VESELOVSKII

Physics Instrumentation Center, Troitsk, Moscow Region, Russia

D. N. WHITEMAN

NASA Goddard Space Flight Center, Greenbelt, Maryland

A. KOLGOTIN

Physics Instrumentation Center, Troitsk, Moscow Region, Russia

E. ANDREWS

CIRES, University of Colorado, Boulder, Colorado

M. KORENSKII

Physics Instrumentation Center, Troitsk, Moscow Region, Russia

(Manuscript received 13 November 2008, in final form 21 February 2009)

ABSTRACT

The feasibility of using a multiwavelength Mie–Raman lidar based on a tripled Nd:YAG laser for profiling aerosol physical parameters in the planetary boundary layer (PBL) under varying conditions of relative humidity (RH) is studied. The lidar quantifies three aerosol backscattering and two extinction coefficients and from these optical data the particle parameters such as concentration, size, and complex refractive index are retrieved through inversion with regularization. The column-integrated, lidar-derived parameters are compared with results from the AERONET sun photometer. The lidar and sun photometer agree well in the characterization of the fine-mode parameters, however the lidar shows less sensitivity to coarse mode. The lidar results reveal a strong dependence of particle properties on RH. The height regions with enhanced RH are characterized by an increase of backscattering and extinction coefficient and a decrease in the Ångström exponent coinciding with an increase in the particle size. The hygroscopic growth factor calculated for a select case is consistent with previous literature results despite the lack of collocated radiosonde data. These results demonstrate the potential of the multiwavelength Raman lidar technique for the study of aerosol humidification process.

1. Introduction

The radiation balance of the earth is strongly influenced by atmospheric aerosols of natural and anthropogenic origin (D'Almeida et al. 1991; Pilinis et al. 1995). For accurate modeling of corresponding radiative forcing, knowledge of the vertical distribution of particle macro- and microphysical parameters is needed. During recent years ground-based and airborne lidars have become important tools for profiling tropospheric aerosols using either single or multiple wavelengths (Kovalev and Eichinger 2004). For quantitative studies of the optical properties of tropospheric aerosol, Raman lidars have proven to be most useful (Ansmann et al. 1992; Ferrare et al. 1998a,b; Ansmann et al. 2000; Turner et al. 2002). This lidar type measures elastically backscattered light simultaneously with Raman backscatter from molecules (nitrogen or oxygen), thus allowing independent calculation of particle backscattering and extinction coefficients without the need for

Corresponding author address: I. A. Veselovskii, Physics Instrumentation Center, Troitsk, Moscow Region 142190, Russia.
E-mail: igorv@pic.troitsk.ru

DOI: 10.1175/2009JTECHA1254.1

critical assumptions about atmospheric parameters. Still, to invert the measured aerosol scattering coefficients to the particle microphysical parameters when only a single output wavelength is used, physical models with numerous a priori assumptions are generally needed.

On the other hand, the application of multiwavelength (MW) Raman lidar can be used to quantify the main particle microphysical parameters with fewer a priori assumptions. Information on the particle extinction and backscatter coefficients at multiple wavelengths is produced by such lidars and, with this information, microphysical properties of aerosols can be retrieved through mathematical inversion (Müller et al. 1999; Veselovskii et al. 2002). Theoretical and experimental studies performed during the last decade have demonstrated that the MW lidar technique is able to provide comprehensive information about aerosol microphysical parameters (Müller et al. 2004, 2005; Veselovskii et al. 2004, 2005), although simulation studies have shown a decreasing sensitivity as particle size increases. These results demonstrate that the key to the successful retrieval of aerosol parameters is the joint use of aerosol backscattering and extinction coefficients, which can be accomplished through the use of Raman or high–spectral resolution methods (Shipley et al. 1983; Liu et al. 2002). Another important finding is that a simplified multiwavelength Raman lidar based on a frequency-tripled Nd:YAG laser can be used to quantify the particle size distribution (PSD) and complex refractive index (Müller et al. 2001; Veselovskii et al. 2004, 2005).

To validate this technique further, the lidar-derived parameters should be compared with comparable results from other instruments. One of the recognized instruments for retrieval of column-integrated aerosol properties is the robotic sun photometer (SP) that is used in the network called AERONET (Holben et al. 1998; Dubovik et al. 2002). The comparison of lidar and sun photometer data has been performed in previous publications (Müller et al. 2004; Balis et al. 2003) as a method to assess the performance of the multiwavelength lidar technique. We also compare lidar-derived results with sun photometer measurements; however we emphasize the height variation under different atmospheric conditions revealed by lidar versus the column-integrated quantities measured by the sun photometer.

One of the key factors influencing the scattering properties of aerosols is their hygroscopicity. As the relative humidity (RH) rises, the uptake of water vapor by hygroscopic aerosols increases the particle size, which generally leads to an increase in light scattering (Hänel 1976). Numerous experimental studies of the relationship between aerosol scattering and relative humidity have been performed in the laboratory with aerosols of known chemical composition (e.g., Tang and Munkelwitz 1993; Fuzzi et al. 2001; Kumar et al. 2003; Svenningsson et al. 2006; Kreidenweis et al. 2006). In situ experiments in the natural environment have also been performed using nephelometers (e.g., Covert et al. 1980; Fitzgerald et al. 1982; Kotchenruther and Hobbs 1998; Kotchenruther et al. 1999; Carrico et al. 2003) and differential mobility analyzers (Radar and McMurray 1986; Swietlicki et al. 2008, and references therein) in tandem with humidity control systems. Under the right conditions, a lidar may provide another tool for studying aerosol hygroscopicity. The advantage of using a lidar (as opposed to laboratory or most in situ studies) is that it can provide relatively continuous altitude-resolved measurements of aerosol properties without perturbing the aerosol or its surroundings. The obvious disadvantage is that, because the aerosol sampled by the lidar is not controlled in any way (source, state, etc.), lidar studies of aerosol hygroscopicity need to be limited to occasions when the same aerosol type exists in at least a portion of a profile that is characterized by widely changing RH so that observed differences in aerosol properties can be attributed primarily to water uptake as RH increases.

The enhancement of lidar backscatter due to particle swelling was first considered by MacKinnon (1969). Since then numerous studies have investigated the relationship between aerosol backscattering and relative humidity (Ferrare et al. 1998b; Pahlow et al. 2006; Wulfmeyer and Feingold 2000; Feingold and Morley 2003; Raut and Chazette 2007; Cuesta et al. 2008). The water vapor mixing ratio in these more recent studies was derived from either lidar measurements, Raman (Ferrare et al. 1998b; Pahlow et al. 2006) and differential absorption (Wulfmeyer and Feingold 2000), or was calculated under a boundary layer cloud deck suggesting a well-mixed boundary layer (Feingold and Morley 2003). If the boundary layer is well mixed, then any change in backscatter in the vertical is considered to be due to the uptake of water vapor by the particles. Assuming the atmosphere is saturated at cloud base and assuming that the potential temperature is constant with height, the relative humidity profile can be calculated (Pahlow et al. 2006; Wulfmeyer and Feingold 2000; Feingold and Morley 2003). Using single-wavelength backscatter lidar data combined with thermodynamic assumptions of the mixing state of the atmosphere allows for the determination of the hygroscopic growth factor $f(\mathrm{RH})$ for relative humidities close to saturation. The growth factor is calculated in terms of backscattering at a given RH, relative to some lower $\mathrm{RH}_{\mathrm{ref}}$. The application of the multiwavelength Raman lidar technique has an advantage over single-wavelength measurements, because it increases the

amount of available information allowing derivation of the particle size distribution and other physical properties along with the water vapor mixing ratio.

The possibility of using the multiwavelength lidar method for the study of cloud condensation nuclei was considered by Feingold and Grund (1994), but experimental implementation of this method is more recent. The increase of particle size and extinction coefficient near the PBL top derived from multiwavelength lidar measurements during the Aerosol Characterization Experiment (ACE 2) field campaign has been reported (Müller et al. 2002; Ansmann et al. 2002). As inversion routines and retrievals improve and additional aerosol products become available (e.g., PSDs, refractive index), the use of multiwavelength lidar to investigate aerosol hygroscopicity may provide new insights into the aerosol properties relevant for climate forcing in the atmosphere.

The goal of this paper is to derive vertical profiles of aerosol physical parameters in the PBL from multiwavelength lidar measurements under varying relative humidity conditions and to compare the column-integrated aerosol parameters with results from the AERONET sun photometer. To demonstrate the potential of the multiwavelength technique to study aerosol hygroscopic growth, data selection techniques are used to assess the mixing of aerosols in the PBL and hygroscopic growth factors are calculated for the best of these cases.

2. Lidar system description

The experiments described here were performed with a multiwavelength Mie–Raman lidar developed at the National Aeronautics and Space Administration (NASA) Goddard Space Flight Center (GSFC). The lidar is based on a Continuum 9050 laser with a 50-Hz repetition rate. The output powers at $\lambda = 355$, 532, and 1064 nm were 17.5, 7.5, and 14 W, respectively. The backscattered light was collected by a Meade LPX200 40-cm aperture Schmidt–Cassegrain telescope operated at 0.35-mrad field of view and inclined so that the elevation angle was 18°. The off-vertical measurements obtained through this approach improve the extraction of parameters in the PBL by decreasing the altitude to which the lidar overlap function influences the retrievals. The collected light passes through an optical fiber to a receiving module, which includes an off-axis parabolic mirror for collimation. The spectral components of the collimated optical signal are separated by dichroic beam splitters and interference filters. In the current configuration the system is capable of detecting three backscattered and two nitrogen Raman signals at $\lambda_R = 387$ and 607 nm. The receiving module also has the ability to measure the water vapor and liquid water from Raman signals at 407.5 and 402 nm, respectively (Whiteman and Melfi 1999), although no liquid water data are analyzed here. The detection in the 355–532-nm range is performed with Hamamatsu R1924 photomultipliers (PMTs); for the 607-nm channel a Hamamatsu H7422P-40 module is used; and backscatter at 1064 nm is measured with an IR-enhanced Si avalanche photodiode (APD) (Licel APD-3.0) operating in analog mode. The outputs of the detectors are recorded at 7.5-m range resolution with a Licel data acquisition system that incorporates both analog and photon-counting electronics.

3. Raman lidar calculation techniques

The combined use of Rayleigh–Mie and Raman backscatters allows independent calculation of the particle backscattering β and extinction α coefficients at 355 and 532 nm (Ansmann et al. 1992). Computation of β_{1064} is performed from the backscattered signal using the following form of the lidar equation:

$$P_\lambda(z) = A_\lambda \frac{1}{z^2}[\beta_\lambda^m(z) + \beta_\lambda^a(z)] \times \exp\left\{-2\int_0^z [\alpha_\lambda^m(z) + \alpha_\lambda^a(z)]\,dz\right\} \quad (1)$$

with the boundary condition of $\beta_\lambda^a(z_{\text{ref}}) = 0$, where $P_\lambda(z)$ is the backscattered power, A_λ is a range-independent calibration parameter, and β_λ^m, β_λ^a, α_λ^m, α_λ^a are molecular (Rayleigh) and aerosol backscattering and extinction coefficients at wavelength λ. The temperature dependence of Raman scattering has been neglected in these calculations because of the relatively mild change in atmospheric temperature over the altitude ranges involved (Whiteman 2003a,b). The extinction profile at 1064 nm is derived by extrapolating Raman measurements at 532 nm through the relationship $\alpha_{\lambda_1}^a/\alpha_{\lambda_2}^a = (\lambda_2/\lambda_1)^k$, where the Ångström coefficient k is calculated from the $\alpha_{355}/\alpha_{532}$ ratio obtained from the lidar data and assumed constant over the wavelength range. The reference distance z_{ref} is chosen above the PBL top where aerosol contribution to backscatter is negligible. A typical lidar signal at 1064 nm is presented in Fig. 1. It shows that for distance $z_{\text{ref}} > 14$ km (for height above 4.2 km) the lidar signal is mainly due to molecular scattering.

The sensitivity of the calculated backscatter and extinction coefficients to the Ångström coefficient, k, is generally mild (Whiteman 2003a) when using the standard Raman lidar technique (Whiteman et al. 1992).

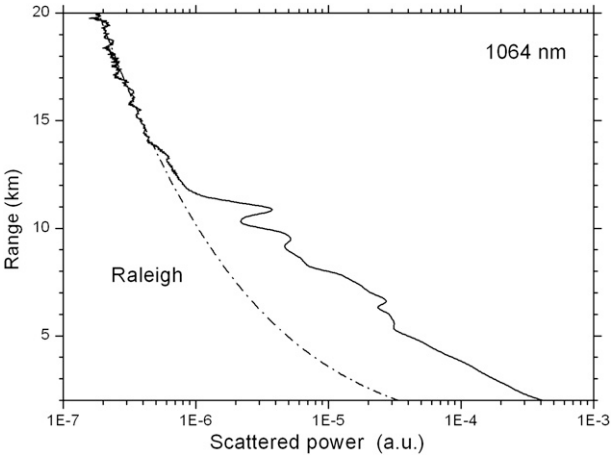

FIG. 1. Lidar signal at 1064 nm measured on 2 Sep 2006 together with simulated Rayleigh signal (dash–dot).

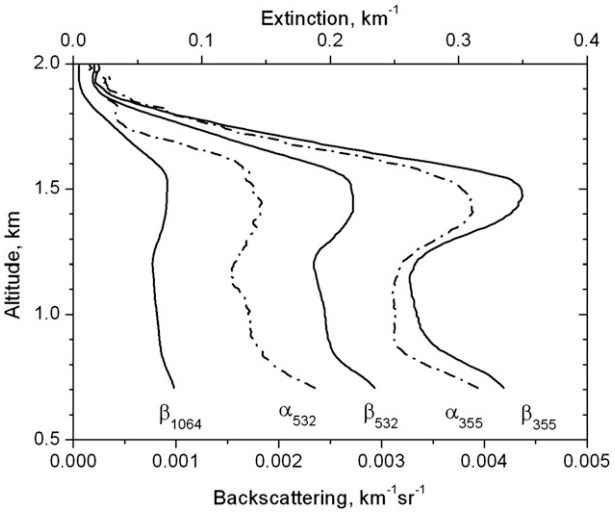

FIG. 2. Vertical profiles of aerosol backscattering (solid) and extinction (dash–dot) coefficients at 355, 532, and 1064 nm measured on 22 Aug 2006.

However, these previous results refer to soundings acquired vertically. For small sounding angles with respect to the horizon, the optical depth of the sounding path is increased significantly and so is the sensitivity to k and its range dependence $k(z)$. It should be mentioned that the Ångström coefficient affects extinction and backscattering in different ways. The uncertainty in the extinction $\alpha_\lambda^a(z) \sim [1 + (\lambda/\lambda_R)^{k(z)}]^{-1}$, where λ_R is the wavelength of the Raman scattered signal, is determined by the fully propagated uncertainties in $k(z)$. The backscattering coefficient $\beta_\lambda^a(z) \sim \exp\{\int_{z_{\text{ref}}}^{z} \alpha_\lambda^a(\xi)[1 - (\lambda/\lambda_R)^{k(\xi)}]\, d\xi\}$ and the uncertainties are integrated when moving away from the reference point. In our computations we use the range-dependent Ångström coefficient $k(z)$ derived from the extinction ratio $\alpha_{355}/\alpha_{532}$ and neglect the spectral variation of k. From the computations performed for different k we conclude that the extinction is not very sensitive to variations in k, with corresponding uncertainties generally being less than 4%. However, for backscattering the use of a range-dependent k is essential. For some cases studied here, the uncertainty in the retrieval of β_{355} at a height $h = 500$ m can increase by as much as 10% if the range variation in k is not considered. When calculating β_{1064}, the approximation that k is spectrally independent in the 532–1064-nm range may appear too coarse. However, the aerosol extinction at 1064 nm is much lower than at 532 nm, so the backscattering at 1064 nm is not very sensitive to spectral or range variations of the Ångström coeffici ent. Based on these considerations, we estimate the uncertainty of both the backscattering and extinction calculation inside PBL to be less than 10%. Typical vertical profiles of backscattering and extinction coefficients at different wavelengths measured on 22 August are shown in Fig. 2.

4. Retrieval of particle microphysical parameters

The lidar-derived backscattering and extinction coefficients are then used to calculate aerosol microphysical properties through inversion. The main features of our retrieval algorithm, which is based on inversion with regularization (Twomey 1977; Tikhonov and Arsenin 1977), are presented elsewhere (Veselovskii et al. 2002, 2004). The only constraints on the permitted refractive index and particle size distribution are that the refractive index is considered to be wavelength independent and that the concentration of the particles with radii below some $r_{\min}$ and above some $r_{\max}$ is zero, where the values of these radii are found in the process of inversion. Furthermore, in the retrieval we do not consider particles outside the radii interval 0.05–10 μm (i.e., these are the limiting values of $r_{\min}$ and $r_{\max}$).

The algorithm was initially designed for retrievals at a single height layer, but in data analysis usually the whole vertical profile of particle parameters is desired. In principle, the profile can be obtained from the retrievals at every layer, though such a procedure is time consuming and does not take into consideration the likely interdependence of aerosol properties between two closely spaced layers. In the new version of the algorithm we have introduced modifications to process all layers simultaneously.

At any height layer the measured optical data g_i (backscattering or extinction) are related to the size distribution $f(r)$ through the Fredholm integral equation:

$$\int_{r_{\min}}^{r_{\max}} K_i(m, \lambda, r) f(r)\, dr = g_i \quad i = -1, \ldots, L, \quad (2)$$

where $K_i(m, r, \lambda)$ are the kernel functions for refractive index m and wavelength λ calculated with Mie theory. Particle size distribution is approximated by the superposition of base functions $B_j(r)$ as

$$f(r) = \sum_{j=1}^{q} c_j(z) B_j(r), \quad (3)$$

where $c_j(z)$ are the weight coefficients. The base functions have a triangular shape on a logarithmic-equidistant grid across the chosen radius interval $[r_{\min}, r_{\max}]$ in which the inversion is performed. The number of base functions in our retrievals is equal to the number of optical data ($q = L = 5$).

The integral Eq. (2) transforms to a linear one as follows:

$$g_i = \sum_{j=1}^{q} A_{ij} c_j, \quad (4)$$

where the elements of weight matrix $\mathbf{A}$ are calculated as

$$A_{ij} = \int_{r_{\min}}^{r_{\max}} K_i(m, \lambda, r) B_j(r)\, dr. \quad (5)$$

At any of l height layers the expression (4) can be written in matrix–vector form as

$$\mathbf{A}^l \mathbf{c}^l = \mathbf{g}^l \quad l = 1, \ldots, \mathrm{N}_L, \quad (6)$$

or it can be expressed in more general form for the whole height range:

$$\mathbf{AC} = \mathbf{G}. \quad (7)$$

In the new version of the algorithm Eq. (7) is solved for all layers simultaneously by means of inversion with regularization:

$$\mathbf{C} = (\mathbf{A}^{\mathrm{T}}\mathbf{A} + \gamma\mathbf{H})^{-1}\mathbf{A}^{\mathrm{T}}\mathbf{G}, \quad (8)$$

where γ is the regularization parameter. Matrices $\mathbf{A}$, $\mathbf{H}$ and vectors $\mathbf{C}$, $\mathbf{G}$ have the following structure (Kolgotin and Müller 2008):

$$\mathbf{A} = \begin{bmatrix} [\mathbf{A}^{(1)}]_{L\times q} & O & \ldots & O \\ O & [\mathbf{A}^{(2)}]_{L\times q} & \ldots & O \\ \ldots & \ldots & \ldots & \ldots \\ O & O & \ldots & [\mathbf{A}^{(N_L)}]_{L\times q} \end{bmatrix}_{N_L L\times q N_L}, \quad (9)$$

$$\mathbf{H} = \begin{bmatrix} [\mathbf{H}^{(1)}]_{q\times q} & O & \ldots & O \\ O & [\mathbf{H}^{(2)}]_{q\times q} & \ldots & O \\ \ldots & \ldots & \ldots & \ldots \\ O & O & \ldots & [\mathbf{H}^{(N_L)}]_{q\times q} \end{bmatrix}_{[qN_L]\times[qN_L]}, \quad (10)$$

$$\mathbf{G} = \left([\mathbf{g}^{(1)}]_{L\times 1} \,|\, [\mathbf{g}^{(2)}]_{L\times 1} \,|\, \ldots \,|\, [\mathbf{g}^{(N_L)}]_{L\times 1}\right)^{\mathrm{T}}_{N_L L\times 1} \quad (11)$$

The regularization parameter is determined from the minimum of modified discrepancy (Veselovskii et al. 2002); $\mathbf{H}$ is the smoothing matrix of second differences (Twomey 1977). The description of how a solution for each layer is generated is presented in our publication (Veselovskii et al. 2002).

As we have mentioned above, the particle size distribution is approximated by five base functions; thus in the absence of a priori information about the particle refractive index the number of retrieved parameters for each layer is larger than the number of observations. This makes the equation system (6) underdetermined. To narrow down the solution range and thus to stabilize the inversion, averaging of solutions in the vicinity of the minimum of discrepancy is used. The details of this approach are presented in our previous publications (Veselovskii et al. 2002, 2004). In the previous version of the algorithm the choice of the averaging interval was made for each layer separately. In the new version used here, all layers are processed simultaneously. The procedure includes the following steps:

- For every kth solution the discrepancy ρ_k is calculated (Veselovskii et al. 2002, 2004). At each height layer the solutions are ordered in accordance with their discrepancy ρ_k, from smallest discrepancy to largest discrepancy.
- At every height layer we calculate the discrepancy $\tilde{\rho}^{(l)}(n_k)$ for the first n_k averaged solutions.
- The total discrepancy for the whole height profile is then calculated as

$$\tilde{\rho}^{\mathrm{tot}}(n_k) \approx \left(\frac{1}{N_L}\right) \sum_{l=1}^{N_L} \tilde{\rho}^{(l)}(n_k). \quad (12)$$

To estimate the number of solutions to be averaged it is convenient to consider the dependence of $\tilde{\rho}^{\mathrm{tot}}$ on the

individual ρ_k [i.e., $\tilde{\rho}^{\text{tot}}(\rho_k)$]. Thus at every layer we sum the solutions with discrepancy smaller than ρ_k. The analysis of the function $\tilde{\rho}^{\text{tot}}(\rho_k)$ permits the determination of the optimal solution set for all layers simultaneously where in general the optimum ρ_k yields a stable $\tilde{\rho}^{\text{tot}}(\rho_k)$ such that the increase of ρ_k does not lead to a significant change in the derived microphysical parameters.

The typical uncertainties of the retrievals studied here were estimated from modeling and from the scatter of the individual solutions to be 20% for volume density and effective radius, 25% for mean radius, and 40% for number density. These uncertainty values are applied as typical throughout all cases and will be represented by the error bars on the solutions.

5. Site and measurement characteristics

The measurements analyzed here were performed during August and September 2006 at NASA GSFC (38.99°N, −76.84°W). This season in the vicinity of Washington, D.C., is frequently characterized by hazy, high-humidity conditions and thus provides an excellent opportunity for the study of aerosol growth due to humidification. Such conditions are also advantageous for the comparison of lidar with sun photometer for three reasons: (i) the majority of aerosols are concentrated inside the planetary boundary layer, (ii) the humidity conditions ensure that particles are reasonably spherical, and (iii) fine mode dominates the PSD (Dubovik et al. 2002).

For studying particle variation within the PBL it is desirable to perform the measurements starting from low altitudes. Therefore, as mentioned before, the lidar system was operated at an angle of 18° with respect to the horizontal so as to minimize the vertically resolved height to which the measurements were influenced by the lidar overlap function. Using this approach, backscattering and extinction coefficients could be calculated starting from an altitude as low as 0.5 km above ground level. Measurements were performed during the nighttime, between 9 and 10 p.m. local time (0100–0200 UT), which was approximately 2 h later than the last sun photometer measurement and approximately 1 h past twilight.

Particle behavior as a function of RH is dependent upon composition and may range from hydrophobic to strongly hygroscopic with monotonic (smoothly varying) or deliquescent (step change) growth. Ambient aerosols typically found in the NASA GSFC area consist mainly of sulfate material (Dubovik et al. 2002; Chen et al. 2002) and therefore significant growth of the particles can be expected for RH $>$ ~80%. Laboratory studies of sulfate-containing particles (Tang 1996) and field studies in the vicinity of NASA GSFC bear this out (Kotchenruther et al. 1999; Fitzgerald et al. 1982). The value of f(RH) (defined as the ratio of total scattering at RH = 85% and 40%, respectively) for typical East Coast regional haze aerosol has been found to be approximately 2.0 (Kotchenruther et al. 1999; Fitzgerald et al. 1982). Increases in aerosol size over the same humidity range are on the order of 1.3 (Fitzgerald et al. 1982).

Profiles of atmospheric density, temperature, and relative humidity were obtained from radiosonde measurements acquired at Dulles Airport, which is located approximately 50 km west of the lidar site. The radiosonde water vapor mixing ratio was calculated from these data using the Wexler formulation for saturation vapor pressure over a liquid surface (Wexler 1976). The radiosondes were launched at 00 UT, which was approximately 1–2 h prior to the time of the lidar measurements. The radiosonde-derived water vapor mixing ratio data were used for the absolute calibration of the lidar water vapor mixing ratio measurements, which were calculated using the traditional Raman lidar technique (Whiteman et al. 1992, 2007). The relative humidity used in the analysis of hygroscopic growth was calculated using the temperature data from the radiosonde and water vapor mixing ratio derived from the lidar measurements.

6. Data selection techniques and day-by-day examples

Multiwavelength lidar retrievals of aerosol properties are considered here on 3 days with differing relative humidity conditions: 1 day with low RH (16 August 2006) and 2 days with high RH (27 August and 12 September 2006). For these latter two cases, the possibility that the measurements reveal growth of a fixed aerosol mixture because of the hygroscopic uptake of water is investigated. A necessary condition for studying hygroscopic growth in the atmosphere using lidar is that the same aerosol mixture exists at all altitudes being studied. This is achieved when the atmosphere is well mixed through convection or if similar aerosols are transported to the measurement site. With similar aerosols being present throughout a profile, any changes in particle size due to changes in RH can be attributed to water uptake or release by the aerosols and hygroscopic growth curves can potentially be calculated.

We used a variety of tools to determine whether well-mixed conditions of aerosols were expected to exist within the lidar profile. Back trajectory analysis was used to determine the source region of the aerosols as a function of altitude. If the source region for the aerosols

was independent of altitude for a given case, we took this to be evidence of a similar aerosol type existing in the lidar profiles. We also took the presence of an altitude-independent, lidar-derived water vapor mixing ratio to be an indication of well-mixed conditions. Finally, we investigated the derived number density from the lidar itself. If this did not vary beyond the uncertainty bars of the retrieval, we also took this to be an indication of well-mixed conditions. We considered all three of these tests for the cases to be presented in the next section. As we will show, two of the three datasets, those of 27 August and 12 September 2006, were found to present a fixed aerosol mixture in a region of the profile. However, only the latter case also provided the range of RHs needed to study hygroscopic growth. The weakness of the analysis presented here is that the temperature data used to convert the lidar mixing ratio into RH were provided by a radiosonde launched approximately 50 km from the lidar site. This introduces sufficient uncertainty in the temperature profile at the lidar site; the hygroscopic growth curves calculated here can only be taken as indicative of the potential of the multiwavelength technique.

a. Measurements from 16 August 2006

This day was characterized by low humidity and the absence of clouds. Figure 3a shows the vertical profiles of water vapor mixing ratio obtained from the lidar and radiosonde measurements. The shapes of the profiles are similar, supporting the use of the sonde data for calibration of the lidar water vapor mixing ratio. It also suggests that the meteorological conditions were similar between the location of the sonde launch and the lidar site. From this point forward in the manuscript, profiles will be shown with respect to the vertically resolved altitude h.

The lidar-derived RH profile agrees quite well with the sonde data, as is shown in Fig. 3a. The RH on 16 August was below 65% in the height interval of 1.0–1.8 km, so enhancement of aerosol extinction due to particle hygroscopicity is expected to be small. The altitude dependence of aerosol properties measured and derived from the lidar on 16 August 2006 is shown in Figs. 3b–e. The top of the boundary layer is at ~1.9 km and it coincides with the drop of water vapor content. Both extinction and backscattering have a secondary maximum near the PBL top likely due to accumulation of aerosols. The Ångström exponent is found to rise with height in the PBL, which suggests that higher altitudes are dominated by smaller particles. This is confirmed by Fig. 3c, showing the vertical profiles of mean and effective radius derived from the lidar data. In the interval between

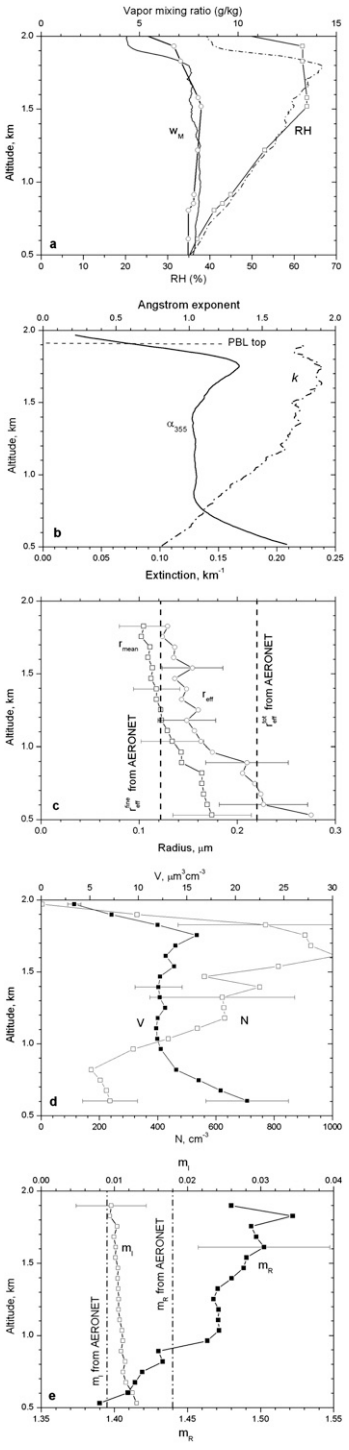

FIG. 3. Vertical profiles of aerosol parameters measured on 16 Aug: (a) water vapor mixing ratio (w_M) and RH derived from the lidar data (solid lines) and from the sonde measurements (line + symbol); (b) aerosol extinction coefficients at 355 nm together with Ångström exponent k; (c) mean r_{mean} and effective r_{eff} radius [dashed line shows the effective radius for the fine mode ($r_{\text{eff}}^{\text{fine}}$) and for the total size distribution ($r_{\text{eff}}^{\text{tot}}$) obtained by AERONET]; (d) number (N) and volume (V) density; and (e) real m_R and imaginary m_I part of refractive index (dotted lines show the results from AERONET).

1.0 and 1.8 km, the retrieved mean radius indicates a decrease in particle size. The lack of particle size increase with height is consistent with RH conditions below the threshold for hygroscopic growth. Figure 3d shows the retrieved number and volume densities on 16 August. From Fig. 3d we conclude that the previously mentioned maximum in particle extinction at ~1.8 km appears to be more likely due to an increase in particle number density than in particle size, though the rise of m_R can be also a contributing factor.

Because 16 August was cloudless it provided a good opportunity to compare the lidar and sun photometer retrievals. The column-integrated particle parameters derived from AERONET (level-1.5 data) and lidar measurements are summarized in Table 1. The uncertainties of AERONET retrieval are estimated based on former publications (Dubovik et al. 2000). To derive column-integrated particle parameters from lidar data, we summed the PSDs at each height layer assuming that the PSD was constant below the lowest lidar retrieval. From this column-integrated PSD mean, the effective radius and volume density were calculated. To get column-averaged refractive indices, the values of m_R and m_I in each layer were weighted by the volume density of the layer (weighting by extinction yielded similar results):

$$\overline{m} = \frac{\int_0^{h_{\max}} V(h)m(h)\,dh}{\int_0^{h_{\max}} V(h)\,dh}.$$

Aerosol optical thicknesses (AOT) provided by AERONET at 355 and 532 nm are 0.32 ± 0.015 and 0.18 ± 0.009. The corresponding values from lidar are 0.3 ± 0.03 and 0.18 ± 0.018. The agreement is good, keeping in mind that we extrapolated the extinction by assuming that the lowest retrieved lidar extinction value at 500 m was constant down to the surface. The effective radius r_{eff} obtained from the inversion of sun photometer measurements was $r_{\text{eff}}^{\text{tot}} = 0.22 \pm 0.02$ μm for the total particle size distribution and $r_{\text{eff}}^{\text{fine}} = 0.12 \pm 0.01$ μm for the fine mode, while the lidar retrievals for the total PSD show effective radius decreasing with height from 0.28 to 0.12 μm with an uncertainty of 0.04–0.06 μm. The effective radius derived from the height-integrated PSD is 0.21 ± 0.04 μm for the total PSD and 0.15 ± 0.03 μm when only fine mode is considered. The height profiles of real m_R and imaginary m_I parts of refractive index are shown in Fig. 3e. The uncertainty of the refractive index retrieval is estimated to be ±0.05 for the real part and 50% for the imaginary part. On 16 August m_R rises with altitude from 1.4 to 1.5, while m_I stays constant at ~0.01 (within the retrieval uncertainty). The same figure shows m_R and m_I obtained from the sun photometer. The spectral variation of the indices is small according to the sun photometer retrievals: m_R changes from 1.44 to 1.43 and m_I from 0.0087 to 0.0094 in the 440–1020-nm spectral range, supporting the use in this case of a spectrally invariant index of refraction in the lidar retrievals. Height-averaged values of refractive index are $\overline{m}_R = 1.45$ and $\overline{m}_I = 0.01$, which are close to the results from AERONET. From this comparison we can conclude that the height-averaged values for both effective radius and refractive index derived from the lidar are in reasonable agreement with the results of sun photometer measurements.

TABLE 1. Column-integrated aerosol parameters derived from lidar and AERONET on 16 Aug 2006.

Parameter		AERONET	Lidar
AOT	355 nm	0.32 ± 0.015	0.3 ± 0.03
	532 nm	0.18 ± 0.009	0.18 ± 0.018
V^{tot} ($\mu m^3/\mu m^2$)		0.056 ± 0.005	0.035 ± 0.007
V^{fine} ($\mu m^3/\mu m^2$)		0.029 ± 0.004	0.025 ± 0.005
$r_{\text{eff}}^{\text{tot}}$ (μm)		0.22 ± 0.06	0.21 ± 0.04
$r_{\text{eff}}^{\text{fine}}$ (μm)		0.123 ± 0.035	0.15 ± 0.03
m_R		1.44 ± 0.04	1.45 ± 0.05
m_I		0.01 ± 0.003	0.01 ± 0.005

Figure 4 shows the column-integrated PSD provided by the sun photometer. The distribution is bimodal with a maximum at 0.11 μm for fine and at 5 μm for coarse mode. The same figure shows the lidar derived PSDs at the altitudes of 1.1 and 1.7 km. The fine modes retrieved by the two instruments are in reasonable agreement, but the lidar-derived PSD begins to decrease for particles slightly larger than 1 μm while the sun photometer PSD does not peak until ~5 μm. This result could be influenced by the fact that the size retrievals shown in Fig. 4c are increasing as height decreases, implying that larger particles may exist below the 0.5-km lower limit of the lidar retrievals. Another influence is the fact that the lidar retrievals, which use a maximum wavelength of 1064 nm (~1 μm), have decreasing sensitivity to particles with sizes greater than ~2 μm. Simulations (Veselovskii et al. 2004) have shown that the estimation of coarse-mode parameters is possible although additional information such as the use of longer wavelengths would be beneficial to the retrieval.

The columnar volume density from the sun photometer was 0.056 ± 0.005 μm^3 $(\mu m^2)^{-1}$ for total PSD and 0.029 ± 0.004 μm^3 $(\mu m^2)^{-1}$ for the fine mode. The corresponding lidar-derived values are 0.035 ± 0.007 and 0.025 ± 0.005 μm^3 $(\mu m^2)^{-1}$. In accordance with Fig. 4 the main part of the lidar-derived density was

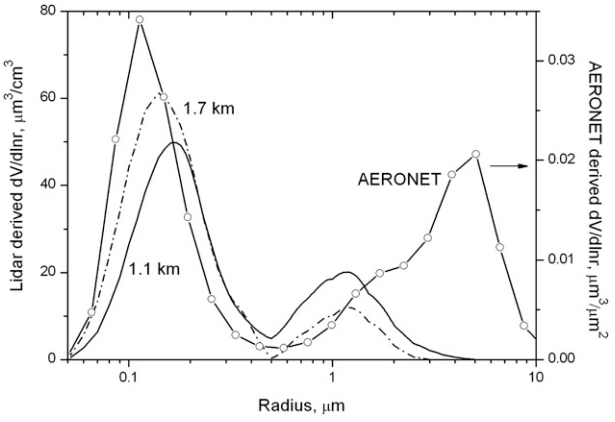

FIG. 4. PSDs derived from lidar measurements at altitudes 1.1 and 1.7 km on 16 Aug. Open symbols show the columnar PSDs from AERONET.

contained in the fine mode and the corresponding value agrees well with the sun photometer measurements.

b. Measurements from 27 August 2006

The measurements on 27 August 2006 were performed under RH conditions sufficiently high to potentially support hygroscopic particle growth studies. At the time of the measurements, however, the back trajectories suggest that three separate air masses were influencing the vertical profile of aerosols present at the lidar site: 1) for the height region of 800–2000 m, the origin of the air was generally southerly, 2) for the height region of 2350–2800 m, the origin was generally south-westerly from the Virginia–Kentucky region, and 3) for the height region of 2950–3400 m, the origin is also to the southwest but from the Alabama–Georgia region. Therefore, without sufficient mixing we would not expect to find the same type of aerosols at all altitudes, thus preventing a clean determination of hygroscopic growth characteristics even if collocated radiosonde temperature data had been available. It should be noted that clouds were present on this day, which prevented sun photometer retrievals, so no comparisons with lidar were possible.

Figure 5 shows the retrievals for 27 August. The top of the boundary layer is at ~3.5 km; the radiosonde- and lidar-measured RH profiles are quite similar and show relative humidity increasing with altitude from values below 50% at the bottom of the lidar retrieval around 500 m to above 90% for altitudes between 2.5 and 3.5 km. The water vapor mixing ratio profile shows a slight decrease with altitude suggesting that the boundary layer may have been well mixed during the daytime but that, at the times and locations of both the sonde launch and

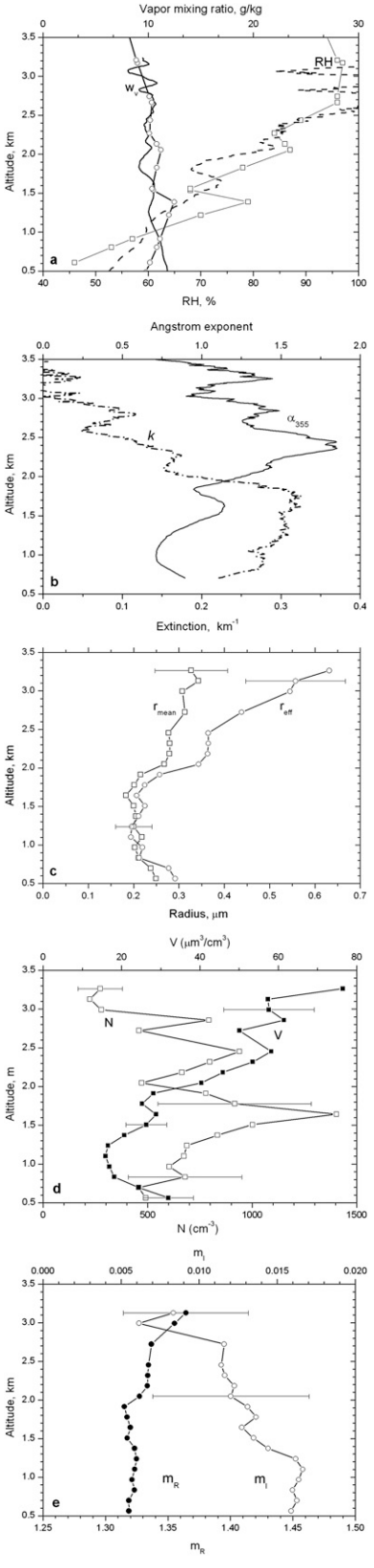

FIG. 5. As in Fig. 3, but for 27 Aug.

the lidar measurements, mixing was not complete in the boundary layer. The incomplete mixing present on this day also makes this a bad case for the study of hygroscopic growth. Nonetheless, the retrievals reveal a strong correlation between particle properties and RH. Inside the altitude range 0.5–1.8 km the particle size decreased slightly with height (Fig. 5c). At an altitude of 1.8 km, RH exceeded 80% and the Ångström exponent at this height starts to decrease from 1.5 to 0, which indicates an increase in particle size as shown in Fig. 5c. A decrease in the Ångström exponent is accompanied by an increase in the particle extinction and backscattering coefficients. The mean and effective radii grow rapidly above 2.0 km reaching 0.30 and 0.6 μm correspondingly. The fast growth of effective radius and volume density in the altitude interval 2.0–3.3 km indicates the appearance of big particles resulting in an increase of extinction. The retrieved m_R on 27 August was very close to that of pure water and varied from 1.32 to 1.36 in the height range considered. The value 1.32 is lower than m_R for water and all common atmospheric aerosols, however uncertainty of retrieval is ± 0.05 and we consider different indices starting from 1.3. The altitude variation in m_R can be considered to be within retrieval uncertainty. The imaginary part decreases above 2.0 km as shown in Fig. 5e. This could be attributable to water uptake in the regions of the aerosol population characterized by higher RH.

c. Measurement from 12 September 2006

In our measurement sessions, high humidity was usually observed during cloudy periods (e.g., 27 August, described above), so there were few opportunities to make a comparison between the lidar retrievals and those of sun photometer. One case where this was possible, however, occurred on 12 September 2006. The profiles of lidar-derived particle parameters for this case are shown in Fig. 6 and the comparison of lidar- and AERONET-derived particle parameters is summarized in Table 2.

The back trajectory analysis for 12 September suggests that for the altitude regions of 1150–2500 m at the lidar site, the origin of the aerosols was from a common region to the NW of the lidar site. We take this to imply that the aerosol mixture between these two altitudes is likely to be the same. This coupled with the wide range of RH present makes this case, of the three presented here, the one most likely to show hygroscopic growth behavior similar to more controlled in situ studies and thus permit hygroscopic growth parameters to be calculated.

The RH shown in Fig. 6 on 12 September exhibited an increase with altitude reaching a maximum at 1.5 km

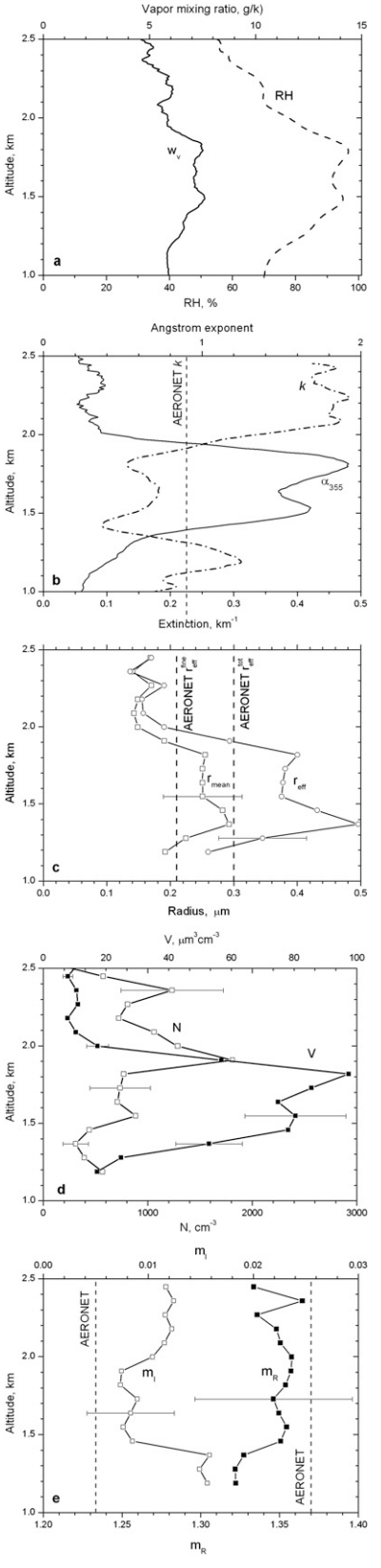

FIG. 6. As in Fig. 3, but for 12 Sep.

TABLE 2. Column-integrated aerosol parameters derived from lidar and AERONET on 12 Sep 2006.

Parameter		AERONET	Lidar
AOT	355 nm	0.38 ± 0.019	0.41 ± 0.08
	532 nm	0.27 ± 0.013	0.31 ± 0.06
V^{tot} ($\mu m^3/\mu m^2$)		0.073 ± 0.007	0.076 ± 0.015
V^{fine} ($\mu m^3/\mu m^2$)		0.05 ± 0.0075	0.057 ± 0.012
r_{eff}^{tot} (μm)		0.301 ± 0.09	0.33 ± 0.07
r_{eff}^{fine} (μm)		0.21 ± 0.06	0.25 ± 0.05
m_R		1.37 ± 0.04	1.34 ± 0.05
m_I		0.005 ± 0.0015	0.009 ± 0.0045

and then decreasing beyond 1.8 km. The radiosonde data indicate saturated conditions between the altitudes of 1.2 and 2.0 km revealing the likely presence of a cloud. The lidar data, however, did not indicate the presence of a cloud, illustrating again the desire to have collocated radiosonde data for studies such as these.

The altitude interval between 1.2 and 2.0 km is characterized by an increase in particle extinction from 0.05 to 0.4 km^{-1} at 355 nm and by a decrease in the Ångström exponent from 1.2 to 0.5 (Fig. 6b). The Ångström exponent derived from the sun photometer at 340-nm and 500-nm wavelengths is approximately 0.9, while the lidar-derived value varies from 0.4 to 1.8. This is another example illustrating that significant changes in particle parameters can occur as a function of altitude that are masked by a column-integrated retrieval from the sun photometer.

The effective radius varies from 0.13 to 0.5 μm while the column-integrated value from the sun photometer is 0.3 ± 0.02 μm. The columnar volume concentrations from the sun photometer when the total PSD and only fine mode is considered are 0.073 ± 0.007 and 0.05 ± 0.0075 μm^3 $(\mu m^2)^{-1}$, respectively. The corresponding lidar-derived values are of 0.076 ± 0.015 and 0.057 ± 0.012 μm^3 $(\mu m^2)^{-1}$. Thus the results from both instruments are in reasonable agreement.

The real part of the lidar-derived refractive index does not change much with altitude and the altitude-averaged value $\overline{m}_R = 1.34 \pm 0.05$ agrees well with the sun photometer result 1.34 ± 0.04. The imaginary part m_I derived from lidar varies with height between 0.015 ± 0.0075 and 0.007 ± 0.0035. The height-averaged value of the imaginary part derived from lidar is $\overline{m}_I = 0.009 \pm 0.0045$, while for the sun photometer $m_I = 0.005 \pm 0.0015$, thus these values are in agreement.

We also studied the correlation between the particle size and the Ångström exponent. Figure 7 shows the dependence of the effective radius on the Ångström exponent for the ensemble of data. There is an inverse dependence of k on r_{eff} that is nearly linear, implying that the lidar-derived k can be used for a preliminary

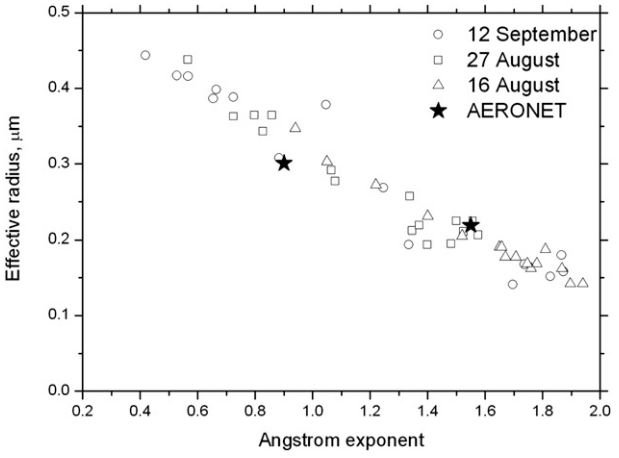

FIG. 7. Correlation between lidar-derived Ångström exponent and effective radius. Solid stars represent the results for AERONET on 16 Aug and 12 Sep.

estimation of particle size. The same figure shows the results for AERONET measurements on 16 August and 12 September. These results are in good agreement with lidar measurements.

7. Potential of multiwavelength lidar for aerosol hygroscopic growth studies

As discussed in the earlier sections, the lidar measurements on 12 September were acquired under conditions considered to be supportive of hygroscopic growth (range of RH and similar aerosol type in the profile) while the data from 27 August were not. We will now consider the impact of RH on the particle parameters for these two cases taking the radiosonde temperature data to represent the temperature structure at the lidar site. The uncertainty in this assumption, due to the separation of the lidar and radiosonde sites, implies that the hygroscopic growth curves calculated from the lidar data should be taken as illustrating the potential of the technique and not as absolute quantifications.

The change of aerosol scattering properties as a function of RH is usually described by the humidification factor (or hygroscopic growth factor) $f(\mathrm{RH})$ used to characterize the response of a homogeneous mixture of aerosols that is subjected to changing values of RH. It is defined as the ratio between extinction of wet and dry aerosol as follows:

$$f(\mathrm{RH}) = \alpha(\mathrm{RH})/\alpha\mathrm{RH}_{\mathrm{ref}}),$$

where $\alpha(\mathrm{RH}_{\mathrm{ref}})$ corresponds to the extinction coefficient at a low, reference RH value, which is obtained at some altitude level. The humidification factor $f(\mathrm{RH})$

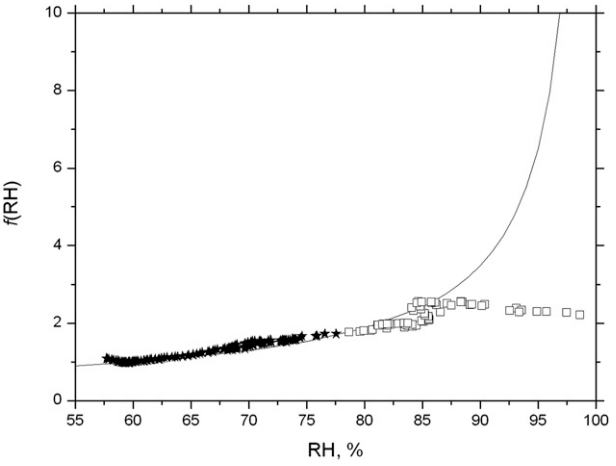

FIG. 8. The f(RH) from the dataset of 27 Aug 2006 for the ranges 800–2000 m (stars) and 2000–2600 m (squares). For these ranges, two distinct source regions for aerosols were identified by back trajectory analysis. Solid line represents the parameterization fit of f(RH) for $g = 0.9$.

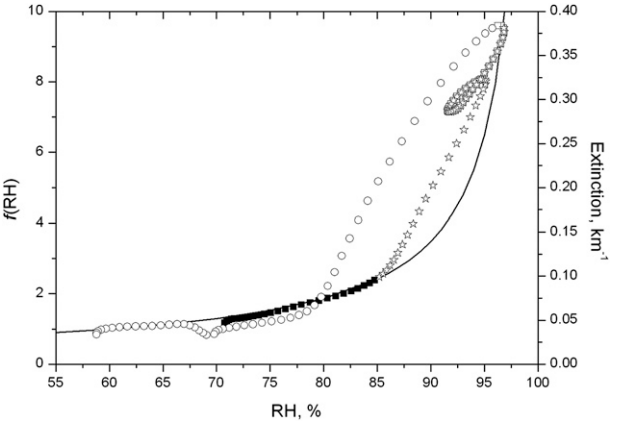

FIG. 9. Dependence of extinction coefficient at 532 nm on RH and humidification factor f(RH) derived from 12 Sep data. Results are shown for altitude ranges: 1.0–1.3 km (solid squares), 1.3–1.8 km (open stars), and 1.8–2.5 km (open circles). Solid line represents the parameterization fit of f(RH) for $g = 0.9$.

can be parameterized using the Hänel model (Hänel 1976), as was done by many investigators (Kotchenruther and Hobbs 1998; Kotchenruther et al. 1999; Raut and Chazette 2007; Randriamiarisoa et al. 2006):

$$\alpha = \alpha_{\text{dry}}(1 - \text{RH})^{-g}, \tag{13}$$

where α_{dry} is the extinction of dry particles. For the reference value of RH this relationship can be rewritten as

$$\frac{\alpha}{\alpha_{\text{ref}}} = \left(\frac{1 - \text{RH}}{1 - \text{RH}_{\text{ref}}}\right)^{-g}. \tag{14}$$

We now calculate f(RH) from the data of 27 August, when different source regions were identified in the data and mixing was incomplete, and 12 September, when the measurement conditions are considered supportive of hygroscopic growth studies. The results for 27 August are shown in Fig. 8 where a reference RH value of 60% was used. A general increase in f is observed with increasing RH, however the curve shows a great deal of scatter and differs significantly from the Hänel model results for $g = 0.9$, which is the best fit for the 12 September results. We take the strong departure of the experimental curve from the simulated curve shown in Fig. 8 to reflect the fact that the conditions present on 27 August were not supportive of hygroscopic growth studies: different source regions of the aerosols were identified along with incomplete mixing indicating the likely presence of different aerosol types as a function of altitude in the profile (though for the first source region, 800–2000 m, the agreement with the model is quite good). However, the general trend of increasing extinction as RH increases is consistent with the retrievals shown in Figs. 5, indicating that changing RH strongly influenced the profile of retrieved parameters.

Considering now data from 12 September, when conditions were more suitable for hygroscopic growth studies, Fig. 9 shows the dependence of extinction coefficient at 532 nm on RH for three altitude ranges. The humidification factor f(RH) is also shown in Fig. 9. Again, the reference value RH_{ref} was chosen to be 60%, because lower values of RH were not accessible in these measurements. The value of f(RH) at RH = 80% in our measurements is 1.78 at 532 nm. Using Fig. 13 in Fitzgerald et al. (1982), an f(RH) at $\lambda \sim 550$ nm for the same humidity range is ~1.45. Using Fig. 5 in Kotchenruther et al. (1999), f(RH) values of ~1.5 and ~1.7 are obtained for clean and anthropogenic-influenced air, respectively, over the same RH range. Thus the obtained values from the lidar are reasonably close to previous results for typical regional haze aerosol on the East Coast.

The best fit to experimental data at 532 nm for RH < 85% is achieved at $g = 0.9$; the corresponding curve is shown in Fig. 9. The derived value of g is in reasonable agreement with earlier studies (Randriamiarisoa et al. 2006) showing variation of this parameter between 0.27 and 1.35. For RH exceeding 85% the lidar-derived humidification factor rises faster than the model prediction. This may be partly contributed by deliquescent growth, which could imply that the simplified parameterization used in expression (15) is insufficient to describe the physics involved and that more complicated models may be needed (Kotchenruther et al. 1999). The hysteresis behavior displayed in Fig. 9 may also indicate the presence of deliquescent compounds in the aerosols

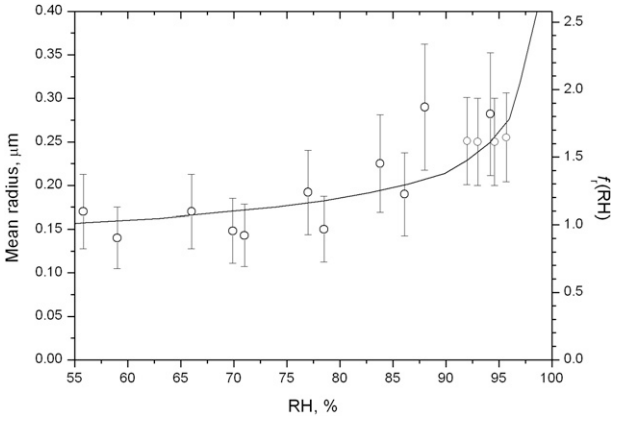

FIG. 10. Dependence of aerosol mean radius on RH derived from 12 Sep 2006 data together with size growth factor f_r(RH). Solid line shows the hygroscopic growth of $(NH_4)_2SO_4$ particle with $r_0 = 0.1$ μm.

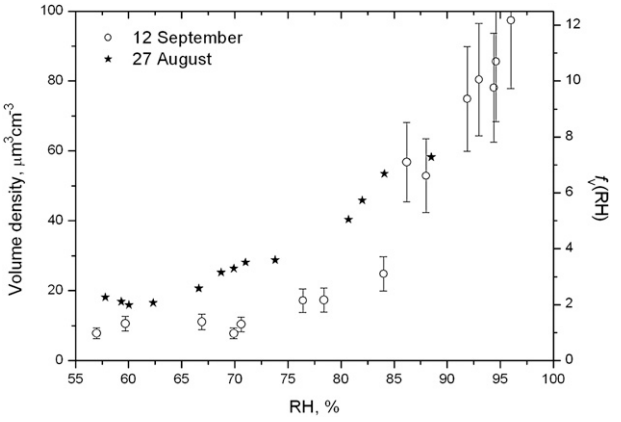

FIG. 11. Dependence of aerosol volume concentration on RH derived from 12 Sep 2006 data together with volume growth factor. For comparison, the results from 27 Aug when the condition of well mixing is not fulfilled are also shown.

(Randriamiarisoa et al. 2006). However, more definitive conclusions about the role of deliquescence in the behavior of these aerosols would require better collocation of temperature and relative humidity measurements with the lidar profiles.

The multiwavelength lidar technique also allows estimation of aerosol size growth factor $f_r(\mathrm{RH}) = r(\mathrm{RH})/r(\mathrm{RH_{ref}})$, which is the ratio between the wet and the quasi-dry particle radius. The dependence of the aerosol mean radius on RH together with size growth factor is shown in Fig. 10. For comparison the same picture shows the hygroscopic growth of ammonium sulfate $(NH_4)_2SO_4$, calculated for the dry particle radius 0.1 μm using the expressions from Tang (1996). Although the scattering of data in Fig. 10 is significant, the value of $f_r(85\%)$ is estimated to be about 1.3, which is a typical number for the East Coast regional haze aerosol (Kotchenruther et al. 1999).

The retrieval of integral particle parameters, such as volume density, is more stable than number density retrievals. Therefore it is interesting to consider the volume growth factor $f_V(\mathrm{RH})$ that may be more appropriate for the study of the hygroscopic growth process using multiwavelength Raman lidar: $f_V(\mathrm{RH}) = V(\mathrm{RH})/V(\mathrm{RH_{ref}})$. Defined this way, $f_V(\mathrm{RH})$ represents the amount of water accepted in the process of particle growth. The corresponding results are shown in Fig. 11. This factor reveals a smoothly varying dependence on RH, which is due to the larger range of volume variation to compare with radius. For comparison, the results from 27 August are also shown. For that day $V(\mathrm{RH})$ does not follow the model curve, which could be another indication of the presence of different aerosol types along the sounding path.

8. Summary and conclusions

The main intention of this paper was to demonstrate the ability of the multiwavelength Raman lidar technique to profile the vertical distribution within the planetary boundary layer of critical aerosol parameters such as mean and effective radius, Ångström exponent, complex refractive index, and number and volume densities under varying relative humidity conditions. A newly designed multiwavelength Raman lidar and upgraded inversion algorithm permits the simultaneous retrieval of microphysical particle parameters at all heights in the profile.

To support the results of the lidar measurements, comparisons with column-averaged quantities from collocated AERONET sun photometer data were performed. The lidar measurements of fine-mode parameters agreed well with the sun photometer, but at present, the lidar technique has difficulty in fully representing the coarse mode. A contributing factor could be that the particles exceeding 2 μm may have been concentrated at altitudes lower than were retrieved by lidar in this study (0.5 km); hence, our next goal is to decrease the minimum useful altitude of the measurements. These comparisons make particularly clear the need to consider the possibility of hygroscopic growth when interpreting AERONET column-averaged data.

Three datasets were studied in detail. One was characterized by low-RH conditions where no evidence of particle growth with increasing RH was observed and two were acquired under higher-RH conditions where a strong correlation was observed between aerosol size and RH. Considering these two latter cases, hygroscopic growth factors were calculated. However, the first of the two cases on 27 August was likely characterized by

differing aerosol mixtures in the vertical while the second case, that on 12 September 2006, was judged to have both a range of RH and a fixed aerosol mixture in a portion of the profile making it suitable for calculations of hygroscopic growth parameters. The calculated hygroscopic growth curves for these two cases differed considerably, with the latter case on 12 September being more consistent with published literature. Regardless of the degree of mixing, the source of aerosols, or other considerations, we found a strong positive correlation between RH and aerosol particle extinction, size, and volume.

The results presented here demonstrate the potential of the multiwavelength lidar technique for the study of aerosol hygroscopic growth in the atmosphere. Although the derived hygroscopic growth parameters agree well with the modeling, they must be considered preliminary because of the lack of temperature data at the lidar site and the inability to fully resolve the coarse mode of the PSD. For validation of the MW technique, the temporal and spatial separation between lidar and radiosonde measurements should be minimized and cases should be selected where the PSD is dominated by the fine mode.

Acknowledgments. We thank the AERONET team of NASA GSFC for help, discussions, and providing us with sun photometer retrievals.

REFERENCES

Ansmann, A., M. Riebesell, U. Wandinger, C. Weitkamp, E. Voss, W. Lahmann, and W. Michaelis, 1992: Combined Raman elastic-backscatter lidar for vertical profiling of moisture, aerosols extinction, backscatter, and lidar ratio. *Appl. Phys.,* **55B,** 18–28.

——, D. Althausen, U. Wandinger, K. Franke, D. Müller, F. Wagner, and J. Heintzenberg, 2000: Vertical profiling of the Indian aerosol plume with six-wavelength lidar during INDOEX: A first case study. *Geophys. Res. Lett.,* **27,** 963–966.

——, F. Wagner, D. Müller, D. Althausen, A. Herber, W. von Hoyningen-Huene, and U. Wandinger, 2002: European pollution outbreaks during ACE 2: Optical particle properties inferred from multiwavelength lidar and star-Sun photometry. *J. Geophys. Res.,* **107,** 4259, doi:10.1029/2001JD001109.

Balis, D. S., and Coauthors, 2003: Raman lidar and sunphotometric measurements of aerosol optical properties over Thessaloniki, Greece during a biomass burning episode. *Atmos. Environ.,* **37,** 4529–4538.

Carrico, C. M., P. Kus, M. J. Rood, P. K. Quinn, and T. S. Bates, 2003: Mixtures of pollution, dust, sea salt, and volcanic aerosol during ACE-Asia: Radiative properties as a function of relative humidity. *J. Geophys. Res.,* **108,** 8650, doi:10.1029/2003JD003405.

Chen, L.-W. A., B. G. Doddridge, R. R. Dickerson, J. C. Chow, and R. C. Henry, 2002: Origins of fine aerosol mass in the Baltimore–Washington corridor: Implications from observation, factor analysis and ensemble air parcel back trajectories. *Atmos. Environ.,* **36,** 4541–4554.

Covert, D. S., A. P. Waggoner, R. E. Weiss, N. C. Ahlquist, and R. J. Charlson, 1980: Atmospheric aerosols, humidity and visibility. *The Character and Origins of Smog Aerosols,* G. M. Hidy et al., Eds., John Wiley and Sons, 776 pp.

Cuesta, J., P. H. Flamant, and C. Flamant, 2008: Synergetic technique combining elastic backscatter lidar data and sunphotometer AERONET inversion for retrieval by layer of aerosol optical and microphysical properties. *Appl. Opt.,* **47,** 4598–4611.

D'Almeida, G. A., P. Koepke, and E. P. Shettle, 1991: *Atmospheric Aerosols: Global Climatology and Radiative Characteristics*. A. Deepak, 561 pp.

Dubovik, O., A. Smirnov, B. N. Holben, M. D. King, Y. J. Kaufman, T. F. Eck, and I. Slutsker, 2000: Accuracy assessment of aerosol optical properties retrieval from AERONET Sun and sky radiance measurements. *J. Geophys. Res.,* **105,** 9791–9806.

——, B. Holben, T. F. Eck, A. Smirnov, Y. Kaufman, M. D. King, D. Tanre, and I. Slutsker, 2002: Variability of absorption and optical properties of key aerosol types observed in worldwide locations. *J. Atmos. Sci.,* **59,** 590–608.

Feingold, G., and C. J. Grund, 1994: Feasibility of using multiwavelength lidar measurements to measure cloud condensation nuclei. *J. Atmos. Oceanic Technol.,* **11,** 1543–1558.

——, and B. Morley, 2003: Aerosol hygroscopic properties as measured by lidar and comparison with in situ measurements. *J. Geophys. Res.,* **108,** 4327, doi:10.1029/2002JD002842.

Ferrare, R. A., S. H. Melfi, D. N. Whiteman, K. D. Evans, R. Leifer, and Y. J. Kaufman, 1998a: Raman lidar measurements of aerosol extinction and backscattering 1. Methods and comparisons. *J. Geophys. Res.,* **103,** 19 663–19 672.

——, ——, ——, ——, M. Poellot, and Y. J. Kaufman, 1998b: Raman lidar measurements of aerosol extinction and backscattering 2. Derivation of aerosol real refractive index, single-scattering albedo, and humidification factor using Raman lidar and aircraft size distribution measurements. *J. Geophys. Res.,* **103,** 19 673–19 690.

——, D. Turner, L. Brasseur, W. Feltz, O. Dubovik, and T. Tooman, 2001: Raman lidar measurements of the aerosol extinction-to-backscatter ratio over the Southern Great Plains. *J. Geophys. Res.,* **106** (D17), 20 333–20 347.

Fitzgerald, J. W., W. A. Hoppel, and M. A. Vietti, 1982: The size and scattering coefficient of urban aerosol particles at Washington, DC as a function of relative humidity. *J. Atmos. Sci.,* **39,** 1838–1852.

Fuzzi, S., S. Decesari, M. C. Facchini, E. Matta, M. Mircea, and E. Tagliavini, 2001: A simplified model of the water soluble organic component of atmospheric aerosols. *Geophys. Res. Lett.,* **28,** 4079–4082.

Hänel, G., 1976: The properties of atmospheric aerosol particles as functions of the relative humidity at thermodynamic equilibrium with the surrounding moist air. *Advances in Geophysics,* Vol. 19, Academic Press, 73–188.

Holben, B. N., and Coauthors, 1998: AERONET: A federated instrument network and data archive for aerosol characterization. *Remote Sens. Environ.,* **66,** 1–16.

Kolgotin, A., and D. Müller, 2008: Theory of inversion with two-dimensional regularization: Profiles of microphysical particle properties derived from multiwavelength lidar measurements. *Appl. Opt.,* **47,** 4472–4490.

Kotchenruther, R. A., and P. V. Hobbs, 1998: Humidification factors of aerosols from biomass burning in Brazil. *J. Geophys. Res.,* **103,** 32 081–32 089.

——, ——, and D. A. Hegg, 1999: Humidification factors for atmospheric aerosols off the mid-Atlantic coast of the United States. *J. Geophys. Res.,* **104** (D2), 2239–2251.

Kovalev, V. A., and W. E. Eichinger, 2004: *Elastic Lidar. Theory, Practice, and Analysis Methods*. Wiley-Interscience, 615 pp.

Kreidenweis, S. M., M. D. Petters, and P. J. DeMott, 2006: Deliquescence-controlled activation of organic aerosols. *Geophys. Res. Lett.,* **33,** L06801, doi:10.1029/2005GL024863.

Kumar, P. P., K. Broekhuizen, and J. P. D. Abbatt, 2003: Organic acids as cloud condensation nuclei: Laboratory studies of highly soluble and insoluble species. *Atmos. Chem. Phys.,* **3,** 509–520.

Liu, Z., N. Sugimoto, and T. Murayama, 2002: Extinction-to-backscatter ratio of Asian dust observed with high-spectral-resolution lidar and Raman lidar. *Appl. Opt.,* **41,** 2760–2767.

MacKinnon, D. J., 1969: The effect of hygroscopic particles on the backscattered power from a laser beam. *J. Atmos. Sci.,* **26,** 500–510.

Müller, D., U. Wandinger, and A. Ansmann, 1999: Microphysical particle parameters from extinction and backscatter lidar data by inversion with regularization: Theory. *Appl. Opt.,* **38,** 2346–2357.

——, ——, D. Althausen, and M. Fiebig, 2001: Comprehensive particle characterization from 3-wavelength Raman lidar observations: Case study. *Appl. Opt.,* **40,** 4863–4869.

——, A. Ansmann, F. Wagner, K. Franke, and D. Althausen, 2002: European pollution outbreaks during ACE 2: Microphysical particle properties and single-scattering albedo inferred from multiwavelength lidar observations. *J. Geophys. Res.,* **107,** 4248, doi:10.1029/2001JD001110.

——, I. Mattis, A. Ansmann, B. Wehner, D. Althausen, U. Wandinger, and O. Dubovik, 2004: Closure study on optical and microphysical properties of a mixed urban and Arctic haze air mass observed with Raman lidar and Sun photometer. *J. Geophys. Res.,* **109,** D13206, doi:10.1029/2003JD004200.

——, ——, U. Wandinger, A. Ansmann, D. Althausen, and A. Stohl, 2005: Raman lidar observations of aged Siberian and Canadian forest fire smoke in the free troposphere over Germany in 2003: Microphysical particle characterization. *J. Geophys. Res.,* **110,** D17201, doi:10.1029/2004JD005756.

Pahlow, M., and Coauthors, 2006: Comparison between lidar and nephelometer measurements of aerosol hygroscopicity at the Southern Great Plains atmospheric radiation measurement site. *J. Geophys. Res.,* **111,** D05S15, doi:10.1029/2004JD005646.

Pilinis, C., S. N. Pandis, and J. H. Seinfeld, 1995: Sensitivity of direct climate forcing by atmospheric aerosols to aerosol size and composition. *J. Geophys. Res.,* **100** (D9), 18 739–18 754.

Radar, D. J., and P. H. McMurray, 1986: Application of the tandem differential mobility analyzer to studies of droplet growth or evaporation. *J. Aerosol Sci.,* **17,** 771–787.

Randriamiarisoa, H., P. Chazette, P. Couvert, J. Sanak, and G. Megie, 2006: Relative humidity impact on aerosol parameters in a Paris suburban area. *Atmos. Chem. Phys.,* **6,** 1389–1407.

Raut, J.-C., and P. Chazette, 2007: Retrieval of aerosol complex refractive index from a synergy between lidar, sun photometer and in situ measurements during LISAIR experiment. *Atmos. Chem. Phys.,* **7,** 2797–2815.

Shipley, S. T., D. H. Tracy, E. W. Eloranta, J. T. Trauger, J. T. Sroga, F. L. Roesler, and J. A. Weinman, 1983: High spectral resolution lidar to measure optical scattering properties of atmospheric aerosols. 1: Theory and instrumentation. *Appl. Opt.,* **23,** 3716–3724.

Svenningsson, B., and Coauthors, 2006: Hygroscopic growth and critical supersaturations for mixed aerosol particles of inorganic and organic compounds of atmospheric relevance. *Atmos. Chem. Phys.,* **6,** 1937–1952.

Swietlicki, E., and Coauthors, 2008: Hygroscopic properties of submicrometer atmospheric aerosol particles measured with H-TDMA instruments in various environments—A review. *Tellus,* **60B,** 432–469.

Tang, I., 1996: Chemical and size effects of hygroscopic aerosol on light scattering coefficients. *J. Geophys. Res.,* **101** (D14), 19 245–19 250.

——, and H. Munkelwitz, 1993: Composition and temperature dependence of the deliquescence properties of hygroscopic aerosols. *Atmos. Environ.,* **27A,** 467–473.

Tikhonov, A. N., and V. Y. Arsenin, 1977: *Solution of Ill-Posed Problems*. Wiley, 272 pp.

Turner, D. D., R. A. Ferrare, L. A. Heilman-Brasseur, W. F. Feltz, and T. P. Tooman, 2002: Automated retrievals of water vapor and aerosol profiles from an operational Raman lidar. *J. Atmos. Oceanic Technol.,* **19,** 37–50.

Twomey, S., 1977: *Introduction to the Mathematics of Inversion in Remote Sensing and Direct Measurements*. Elsevier, 256 pp.

Veselovskii, I., A. Kolgotin, V. Griaznov, D. Müller, U. Wandinger, and D. Whiteman, 2002: Inversion with regularization for the retrieval of tropospheric aerosol parameters from multiwavelength lidar sounding. *Appl. Opt.,* **41,** 3685–3699.

——, ——, ——, ——, K. Franke, and D. N. Whiteman, 2004: Inversion of multiwavelength Raman lidar data for retrieval of bimodal aerosol size distribution. *Appl. Opt.,* **43,** 1180–1195.

——, ——, D. Müller, and D. N. Whiteman, 2005: Information content of multiwavelength lidar data with respect to microphysical particle properties derived from eigenvalue analysis. *Appl. Opt.,* **44,** 5292–5303.

Wexler, A., 1976: Vapor pressure formulation for water in range 0 to 100°C: A revision. *J. Res. Natl. Bur. Stand.,* **80A,** 775–785.

Whiteman, D. N., 2003a: Examination of the traditional Raman lidar technique. I. Evaluating the temperature-dependent lidar equations. *Appl. Opt.,* **42,** 2571–2592.

——, 2003b: Examination of the traditional Raman lidar technique. II. Evaluating the ratios for water vapor and aerosols. *Appl. Opt.,* **42,** 2593–2608.

——, and S. H. Melfi, 1999: Cloud liquid water, mean droplet radius, and number density measurements using a Raman lidar. *J. Geophys. Res.,* **104** (D24), 31 411–31 419.

——, ——, and R. A. Ferrare, 1992: Raman lidar system for the measurement of water vapor and aerosols in the Earth's atmosphere. *Appl. Opt.,* **31,** 3068–3082.

——, I. Veselovskii, M. Cadirola, K. Rush, J. Comer, J. R. Potter, and R. Tola, 2007: Demonstrations measurements of water vapor, cirrus clouds, and carbon dioxide using a high-performance Raman lidar. *J. Atmos. Oceanic Technol.,* **24,** 1377–1388.

Wulfmeyer, V., and G. Feingold, 2000: On the relationship between relative humidity and particle backscattering coefficient in the marine boundary layer determined with differential absorption lidar. *J. Geophys. Res.,* **105,** 4729–4741.